Available online at www.sciencedirect.com

jmr&t Journal of Materials Research and Technology

journal homepage: www.elsevier.com/locate/jmrt

Original Article

Remote laser welding of Zn coated IF steel and 1050 aluminium alloy: processing, microstructure and mechanical properties

H.R. Kotadia [a,b,*], P. Franciosa [b,**], S. Jabar [b], D. Ceglarek [b]

[a] School of Engineering, Liverpool John Moores University, Liverpool, L3 3AF, UK
[b] WMG, University of Warwick, Coventry, CV4 7AL, UK

ARTICLE INFO

Article history:
Received 4 April 2022
Accepted 7 May 2022
Available online 11 May 2022

Keywords:
Dissimilar material welding
Remote laser welding (RLW)
Zn coated IF Steel
1050 aluminium
Intermetallics

ABSTRACT

The integrity of steel-aluminium dissimilar alloy joints is dependent on the intermetallic phases (IMCs) and the extent of the bonding area. The excessive growth of brittle Al_xFe_x IMCs within the weld pool and interfaces is disadvantageous due to the initiation and propagation of hot and cold cracking during the solidification. The purpose of this work was to assess the development of Remote Laser Welded (RLW) joints of Zn coated interstitial free (IF) steel to 1050 aluminium alloy, which can be used in cooling circuits and electrical connectors in automotive applications. Welding experiments with variable RLW parameters (power, welding speed and focal offset) were performed to study the formation of IMCs and impact of joint integrity. Results showed that while in conduction mode (at power densities of 0.13–0.18 MW/cm^2) three IMCs were identified through SEM/EDX and EBSD: $\eta - Al_5Fe_2$, $\kappa - AlFe_3$ and $\theta - Al_{13}Fe_4$ which possessed nano-hardness indentation values of approximately 12, 5 and 5 GPa, respectively; they formed in a non-continuous interfacial layer, the weld pool composition remained homogenous, and cracking was minimal. On the contrary, in keyhole mode (at power densities of 0.16–0.40 MW/cm^2) welded samples produced a continuous and thick IMC layer, continuous and/or excessive cracking and an inhomogeneous weld pool composition due to the excessive mixing of steel and aluminium, of up to 10 wt.% of Al in the weld pool. The nominal lap shear strength for the sample produced in conduction mode was of 77%, with respect to the weakest joint material (Al). This work found a close link between the welding mode and weld pool chemistry which significantly determined the IMCs distribution and thickness, extent of cracking within the weld pool and mechanical properties.

* Corresponding author.
** Corresponding author.
E-mail addresses: h.r.kotadia@ljmu.ac.uk (H.R. Kotadia), P.Franciosa@warwick.ac.uk (P. Franciosa).

https://doi.org/10.1016/j.jmrt.2022.05.041

1. Introduction

The introduction of ever stricter CO_2 emission targets has pushed automotive manufacturers to develop and implement effective solutions to reduce vehicle weight and optimise technical performances, such as driveability and safety. Furthermore, due to the market push for battery electric vehicles (BEVs) and the increase of battery systems and their weight (200–400 kg per vehicle, which is much heavier than a full gas tank in the equivalent internal combustion engine (ICE) vehicles), the development of optimised structures is highly desirable to reduce system cost and meet vehicle performance targets [1]. Recent reports from manufacturers have indicated a common trend towards adopting multi-materials structures as key enablers to ensure the "right material at the right place for the right performance". Aluminium (Al) and Iron (Fe) based alloys are certainly the most adopted alloys for automotive body-in-white construction. It has been reported that 70–80% of automotive body construction is currently made of aluminium alloys (both sheet and extrusion, and casting) [1] and steel grades (from mild to ultra-high strength steel) [2]. Iron based alloys possess versatile mechanical properties such as cost-effective strength, good creep resistance, and formability [3]; while Al alloys provide excellent value in applications where low density and/or good corrosion resistance properties are desired [4]. As a result, the ability to join these two materials is vital for making hybrid components that take advantage of the properties of both materials [5,6]. Examples of such hybrid designs are lightweight body-in-white structures, protective Al coatings on steel sheets or tubes, or heat exchangers in energy conversion systems [7].

The selection of the joining process is crucial and must satisfy both functional requirements to achieve desired joint integrity, but also manufacturing requirements such as capital cost, process flexibility and ease of automation. Various processes have been proposed such as mechanical fastening [8–10], chemical bonding (adhesive) [11], solid state (friction stir [12,13] and ultrasonic [14]) and thermal/fusion joining (arc [15], Resistance Spot Welding (RSW) [16], Electron Beam Welding (EBW) [17], and (Remote) Laser Beam Welding (RLW/LBW) [18–24]). Fusion welding of Fe and Al alloys suffers from excessive growth of brittle Al_xFe_x intermetallic compounds (IMCs) and defects such as hot cracking, and segregation as shown in Fig. 1. The growth and volume of IMCs and defects are largely determined by the reaction conditions (e.g., time/temperature cycle, surface conditions, deformation). A number of studies [6,7,14,18,21] have identified brittle IMC phases such as ζ (Al_2Fe), η (Al_5Fe_2), θ ($Al_{13}Fe_4$) and κ - $AlFe_3$ at the reaction layer and within the weld pool. Although it is thermodynamically possible to produce a range of IMCs in the Al-Fe system, most experimental work on fusion welding confirmed the η phase as the major constituent of the reaction layer [6,7,25], which is widely acknowledged to be caused by its rapid growth kinetics facilitated by an open and anisotropic crystallographic arrangement ($[110]\eta//[111]_{Fe}$, $(110)\eta//(0\bar{1}1)_{Fe}$, $(1\bar{1}0)\eta//(2\bar{1}\bar{1})_{Fe}$) as it facilitates nucleation of the η phase [26]. Therefore, the nucleation and growth of the η phase is of great relevance for dissimilar joining as it has been reported to be one of the most brittle intermetallic phases of the Al–Fe system [6,7,21].

Two main approaches have been explored to improve fusion welding joints of Fe and Al alloys: (i) addition of alloying elements/filler material in the weld pool; and (ii) engineering/modifying the processing conditions to control the weld pool which is suitable for dissimilar metal welding. Silicon (Si) is an effective and commonly added element to retard IMC growth kinetics in Al dip-coatings on steel [27–30]. Silicon is added up to 12 wt.% to specifically supress the brittle η phase thickness. According to Nicholls et al. [31], there is an interaction of Si atoms within the open crystallographic arrangement of the η phase, whilst another hypothesis by Springer et al. [7] suggested that it is due to a reduction of the activation energy. Kurakin [32] noted the formation of a barrier layer in the form of $Al_{1-x-y}Fe_xSi_y$ and suggested that this barrier layer can retard the diffusion of Al atoms. On the other hand, Zinc (Zn) has the opposite effect to Si by increasing interfacial IMCs growth. This growth acceleration was found to be at maximum with additions of 10 wt.% Zn [33]. Springer et al. [6] and Jia et al. [34] suggested that Zn coating on steel can be regarded as beneficial in solid–liquid joining procedures, aiding bonding by rapid dissolution thereby resulting in a controlled formation

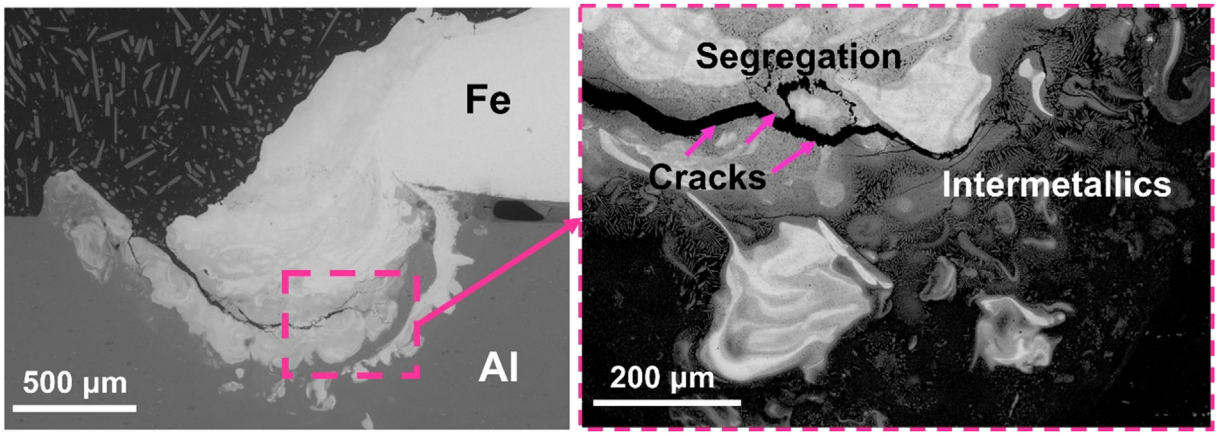

Fig. 1 – SEM micrographs of Steel-Al dissimilar metal weld by using RLW showing hot-cracking and chemical inhomogeneity (segregation) of the weld pool.

Table 1 – Summary of selected papers, which include materials, parameters and mechanical properties of Steel to Al dissimilar metal laser welding.

Materials	Parameters	Weld type	Strength: (σ_{weld}) [N/mm^2]	Strength of weakest joint material (Al): (σ_{Al}) [N/mm^2]	Nominal Strength: ($\sigma_{weld}/\sigma_{Al}$) × 100 [%]	Reference
DP590 steel and AA6061	P: 4 kW, S_x: 40–60 mm/s	Lap joint	90.5	~240	~38	[23]
Steels: HX220LAD+Z100, 22MnB5, 1.4030 and AA6016-T4	P: 3.75 kW	Lap and fillet joints	42.5 and 19.4, respectively	~230	~18 and 8, respectively	[24]
316L ASS and AA6061	P: 0.8–1 kW, S_x: 166.66 mm/s	T-joint	31.038	~240	~13	[35]
XF350 low carbon steel and AA5083-H22	P: 4.46–5.57 kW, S_x: 5–6.66 mm/s	Lap joint	≥62.5	~337	~19	[40]
304L ASS and AA5252	P: 250–472 W, S_x: 11–94 mm/s	Lap joint	≥102.5	~180 N/mm^2	~57	[41]
304L ASS and AA6063	P: 70 W, S_x: 150 mm/s	Lap joint	67.7 at 225 kHz and 56.5 at 325 kHz	~190	~36 and 30	[42]
DP590 steel and AA6061	P: 2.4–4.0 kW, S_x: 5–28.3 mm/s	Lap joint	85	~240	~35	[43]
Q235 steel and AA6061	P: 2 kW, S_x: 45 mm/s	Lap joint	115.6	~240	~48	[44]
316L ASS and AA1060	P: 265–295 W, S_x: 4–10 mm/s	Lap joint	47	~70	~67	[45]
Zn coated IF steel and AA1050	**P: 3.6–5.7 kW, S_x: 23.33–55 mm/s**	**Lap joint**	**105.3**	**~137**	**~77**	**Current Study**

of even and regular reaction layers without defects. It was also noted that the $Al_5Fe_2Zn_{0.4}$ phase (formed through Zn diffusion) was a ductile and tough phase, in comparison with the η-Al_5Fe_2 and κ-$AlFe_3$ IMCs [34]. Furthermore, Li et al. [35] demonstrated through first principle calculations and experiments that the η-Al_5Fe_2 phase has the lowest enthalpy of formation and highest binding energy of the AlFe IMCs.

However, additions of Zn can pose limitations for critical applications by altering steel properties, formation of liquid metal embrittlement (LME) cracking, and increasing costs along with preferential vaporizing of the galvanized layer (Zn) during the fusion welding. An alternative to addressing the inherent limitations of alloying elements/filler material is to optimise welding processing conditions to control the weld pool chemistry, solidification, and interfacial IMCs. In recent years, RLW has gained traction since it is regarded as highly flexible and allows the introduction of sophisticated welding patterns, fast beam re-positioning with superior processing speed, laser power modulation and beam shaping [36,37]. The combination of these features has been successfully demonstrated for welding challenging materials such as non-ferrous alloys and highly reflective materials (copper and wrought aluminium) [38,39]. While the application of RLW to join dissimilar material structures has attracted significant interest, however, the fundamental mechanisms involving the intermetallic phases (IMCs) formation and the relationships with welding parameters are not fully understood. The most specific and recent publications regarding laser welding of Steel and Al are summarised in Table 1.

In light of the existing literature on laser welding, it has become clear that a systematic investigation is required to establish an optimised processing window by using like-for-like industrial scale equipment. Also, in most literature studies [23,24,40–42], the formation of AlFe IMCs and cracks are studied, however, the relationships between the welding mode and weld pool chemistry in the formation of the IMCs are often neglected. The present study focuses on an industrial scale RLW technique by altering process parameters such as laser beam power (P), welding speed (S_x) and focal offset (A_z) which mainly govern the welding mode (conduction and keyhole) and influence the weld pool dynamics. This paper uses detailed microstructural characterisation approaches such as SEM-EDS/EBSD and μ-XRF to understand the mixing behaviour of Fe and Al in different weld geometries. In order to correlate key RLW process parameters to the formation of conduction and keyhole mode welds. This will determine the process parameters which are optimal for producing a weld with minimum mixing between the Fe and Al, with controlled formation of IMCs that as a result, leads to minimum or no cracking with mechanical properties comparable to those found in the literature, i.e., summarised in Table 1.

2. Experimental procedure

The following section provides a detailed description of the RLW procedure as well as metallographic sample preparation, weld characterisation and mechanical properties. Several characterisation techniques were used to analyse the welded joint cross sections. Initial assessments were made using an

optical microscope, followed by detailed electron microscopy on welds of specific interest using SEM/EDS, EBSD and μ-XRF. High speed imaging was used to analyse the weld pools during the RLW procedure. Mechanical testing in the form of a lap shear test was used to compare the strengths of specific welds of interest.

2.1. Materials

RLW was performed between an IF steel coated in Zn and 1050 aluminium alloy with thicknesses of 1 and 3 mm's, respectively, the two sheets were clamped together with no gap. In the current study, leaner alloys were selected rather than the multicomponent alloys, which allows a clear insight into the role of processing conditions on IMCs. The typical application for these two materials in combination is joining of the electrical connections (busbars) made of Al [46] to the steel chassis of the automotive vehicle. Rectangular sheets of 38 mm × 120 mm (coupons) were sectioned using a guillotine cutter from 200 mm × 200 mm industrially supplied rolled sheets. The chemical compositions of the materials used are given in Table 2.

2.2. Remote laser welding (RLW) experiment set-up and procedure

A 6 kW diode laser (Laser Line GmbH, Germany), with a beam parameter product of 6 mm mrad was used for the welding procedure. The laser beam was delivered through an optical fiber of 600 μm in diameter and was coupled with a WeldMaster remote welding head (Precitec GmbH, Germany), which comes with a 150 mm collimating lens, and a 300 mm focal length. The resulting Rayleigh length was 13 mm. No shielding gas nor filler wire was used for the trials. The RLW head was mounted on a six-axis robot system from ABB Robotics. The focal offset, A_z, was measured as the distance along the beam axis between the focal point and the intersection of beam with the part being welded - it is zero when the focal point is on the part surface. All experiments were conducted with a 10° beam incidence angle.

The experimental investigation was carried out by varying laser beam power (P) from 3600 to 5700 W, welding speed (S_x) from 1.4 to 3.3 m/min, and focal offset (A_z) of the upper Fe sheet from 5 to 20 mm. The list of the processing parameters (P, S_x, A_z) are listed in Table 3 and the experimental setup is shown in Fig. 2 including the lap joint configuration. It is also worth noting that the steel sheet was always placed above the Al during each welding trial. The absorptivity of the steel at ambient temperature is 10 times greater than that of Al and consequently, a larger fraction of the incident laser radiation is initially absorbed. In addition, the five times lower thermal conductivity of the steel compared to the Al, leads to a larger fusion zone. Each experiment was repeated twice, and three cross sections of each coupon were used for metallographic study. The continuous wave of the laser can be defined through a series of equations Eqs. (1)–(3) which define the power density (P_d), interaction time of the beam on the metal surface (t) and the specific energy density (E_d). The power density is defined as the (average) laser power (P) per unit area of the laser spot (A_s) which is given in Eq. (1). The interaction time of the beam to metal surface is defined as the laser spot diameter (d) divided by the speed (S) of the laser traversing over the metal surface which is given in Eq. (2). The specific energy density is defined as the product of the (average) laser power and interaction time, divided by the area of the laser spot, which is defined in Eq. (3).

Table 2 – Compositions of the steel and Al sheets as determined through optical emissions spectroscopy (in wt.%).

Fe (IF steel)	Fe	C	Mn	Al	Si	S
	balance	0.05	0.165	0.05	0.03	0.01
Al (1050)	Al	Si	Fe	Cu	Mg	Ti
	balance	0.08	0.47	0.006	0.001	0.025

Table 3 – A list of processing parameters used for the welding trials with the respective power density and specific energy density.

Sample ID	Focal offset A_z (mm)	Speed S_x (m/min)	Power P (W)	Power density P_d (MW/cm^2)	Specific energy density E_d (J/mm^2)
S1	5.0	3.3	4860	0.373	87.33
S2	10	3.3	4860	0.267	73.88
S3	15	1.4	3600	0.134	106.26
S4	15	1.4	3780	0.141	111.58
S5	15	1.4	3960	0.148	116.89
S6	15	1.4	4680	0.174	138.14
S7	15	1.8	4860	0.181	111.58
S8	15	2.2	4860	0.181	91.29
S9	15	3.0	4800	0.179	66.12
S10	15	3.0	4860	0.181	66.95
S11	15	3.0	5100	0.190	70.25
S12	15	3.0	5400	0.201	74.38
S13	16	3.0	5700	0.197	75.56
S14	18	3.0	5700	0.169	70.10
S15	19	3.0	5700	0.157	67.58
S16	20	3.0	5700	0.146	65.20

$$Power\ \ density\ (P_d) = \frac{P}{A_s}\left[MW\,/\,cm^2\right] \tag{1}$$

$$Interaction\ time\ (t) = \frac{d}{S}\ [s] \tag{2}$$

$$Specific\ energy\ density\ (E_d) = P_d \cdot t\,[J\,/\,mm^2] \tag{3}$$

2.3. High-speed imaging

A Photron FASTCAM NOVA S6 camera with Cavilux SmartLaser illumination at 808 nm with an exposure of 20 μs and 40,000 fps was used for the high-speed imaging. The purpose of the high-speed imaging was to further understand the metallurgical changes between conduction and keyhole mode welding, with a real-time high frame rate video due to the extremely high-speed nature of the welding process. As shown in Fig. 2(a), the directions of the laser light source and of the camera optics are in the same plane with the following angular positions and distances: (i) the distance between the optics of the camera and the weld coupon to be welded,

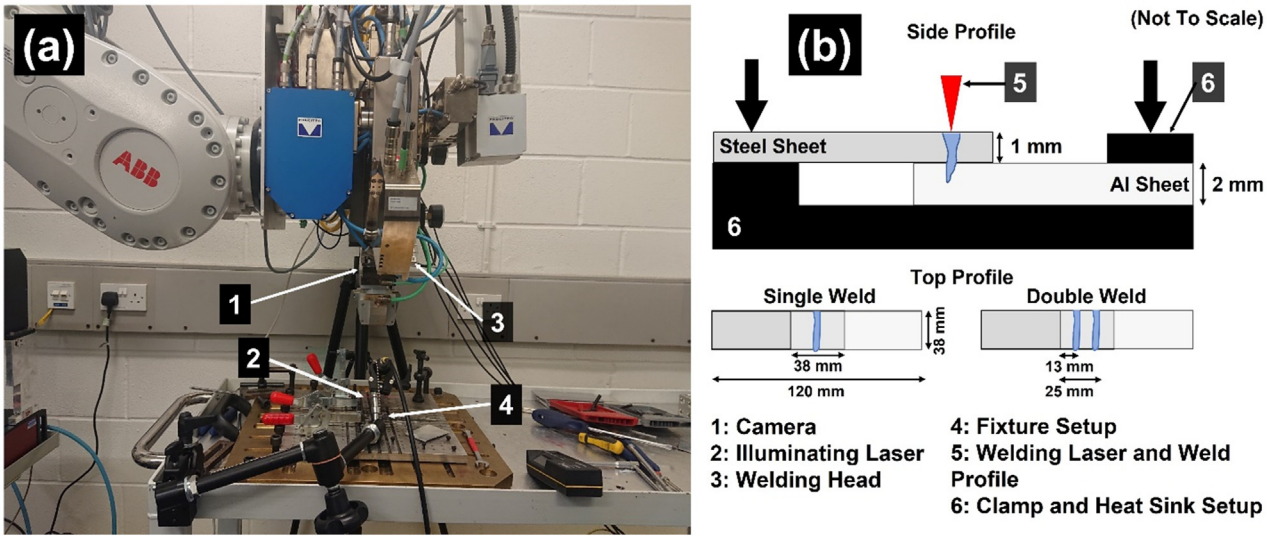

Fig. 2 – Experimental set up: (a) photograph of the setup for the RLW trials and (b) a schematic of the setup used for the RLW welded coupons (Steel-Al) and lap-shear test specimens with a single weld and double weld. (Schematic is not to scale).

$d_1 = 30$ cm; (ii) the distance between the laser light source and the weld coupon to be welded, $d_2 = 12$ cm; (iii) the angular position of the camera, $\theta_1 = 54°$; and, (iv) the angular position of the laser light source, $\theta_2 = 33.5°$. The optical zoom has been set to a value of 3x and the frame resolution in the video was 256×400 pixels.

2.4. *Characterisation and analysis*

Welded samples were prepared for microstructural observations of the cross-sectional area/structure (three different cross sections along the weld length per sample). The samples were sectioned perpendicular to the sheet using a diamond coated blade, with an oil/water solution acting as a coolant and lubricant. Samples were mounted using a conductive bakelite resin and ground and polished using standard metallographic procedures. Initially, key performance indicators (KPI) were measured through the analysis of weld cross-sections using optical and SEM micrographs, via image analysis using commercially available image processing software ImageJ, as schematically is depicted in Fig. 3. These included the weld-pool geometry which included the total weld width and penetration depth, the heat affected zone (HAZ), the IMCs thickness (es), and the total cracking. Average

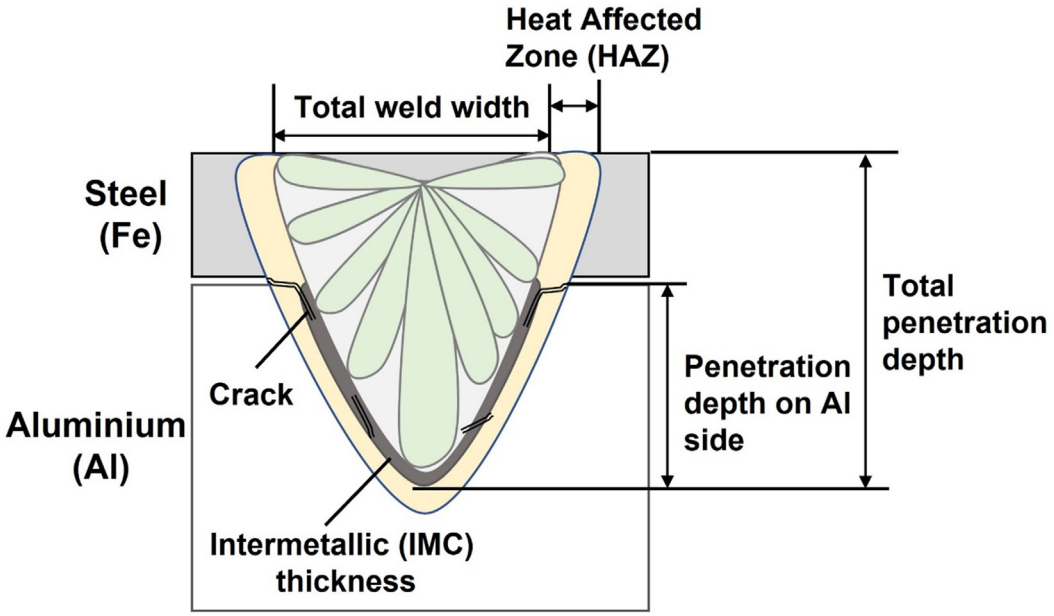

Fig. 3 – Schematic illustration of the weld pool geometry with the key performance indicators (KPIs) labelled which were analysed in this study.

measurements and the standard deviation were acquired from a total of three cross-sections from each weld. In depth analysis on selected samples was performed using a μ-X-ray fluorescence (μ-XRF), and a field emission gun - scanning electron microscope (FEG-SEM) equipped with energy-dispersive X-ray spectroscopy (EDX) and electron backscatter diffraction (EBSD). EDX was used to study the chemistry and composition variation in the weld pool and EBSD was used to study grain orientation and for identifying reaction phases. The μ-XRF was used to chemically map large regions of the weld pool to examine the composition/mixing of the Fe and Al due to the laser welding process.

2.5. *Mechanical testing*

The lap shear mechanical testing was performed on single and double seam welded coupons at a strain rate of $5 \times 10^{-3}\ s^{-1}$ by using an Instron 30 kN tensile testing machine, in accordance with the EN ISO 12273 standard [47], which showed the optimized laser welded process parameters (Sample ID S4, Table 3). It should be noted that for double welded samples, the welds were performed 12 mm apart, taking the centre of the 1st weld as point 0. Two tests were conducted to validate the repeatability of the welded joints. Information on geometry and dimensions of the lap shear test specimen is shown in Fig. 2(b). Nano-indentation of weld interfacial area was performed using a Micro Material NanoTest Vantage with a standard Berkovich tip. The test was carried out using a 10 × 10 grid of indents with a spacing of 10 μm between indents in the x and y directions. The parameters used for the nano-indentation were as follows, a constant load of 5 mN with a dwell time of 10 s at room temperature (22 °C), with a rate of loading of 1 mN/s.

3. Experimental results and discussion

3.1. *Process parameters selection window*

Figures 4 and 5 show SEM micrographs of the weld coupons cross-sections for the welding process parameters as listed in Table 3. The weld coupon cross-sections were evaluated by

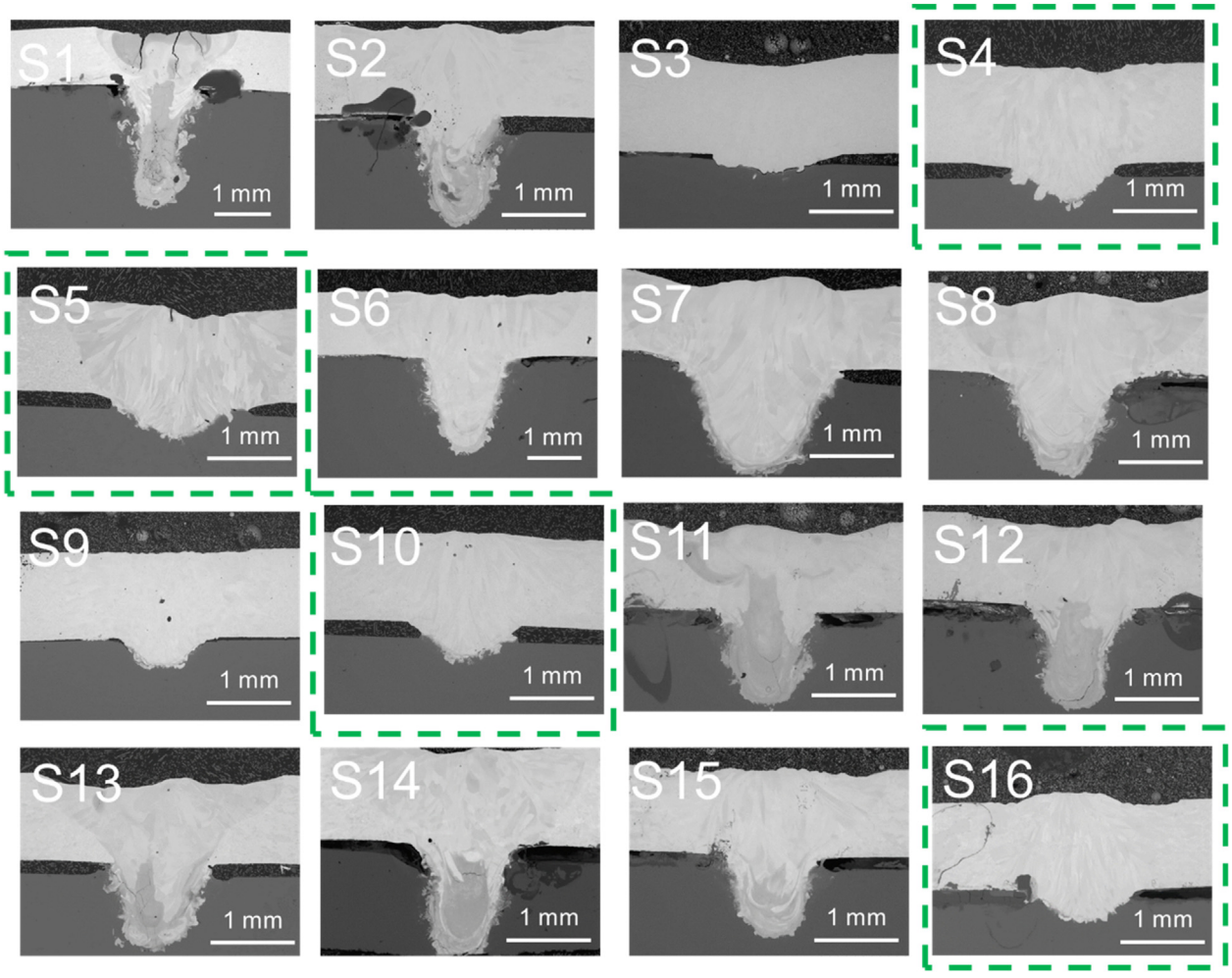

Fig. 4 – SEM micrographs showing the cross sections of the weld pools for each sample, as listed in Table 3. Note: The distinct weld pool geometries with respect to the welding parameters used. Samples S4, S5, S10 and S16 highlighted in green shown little to no cracks.

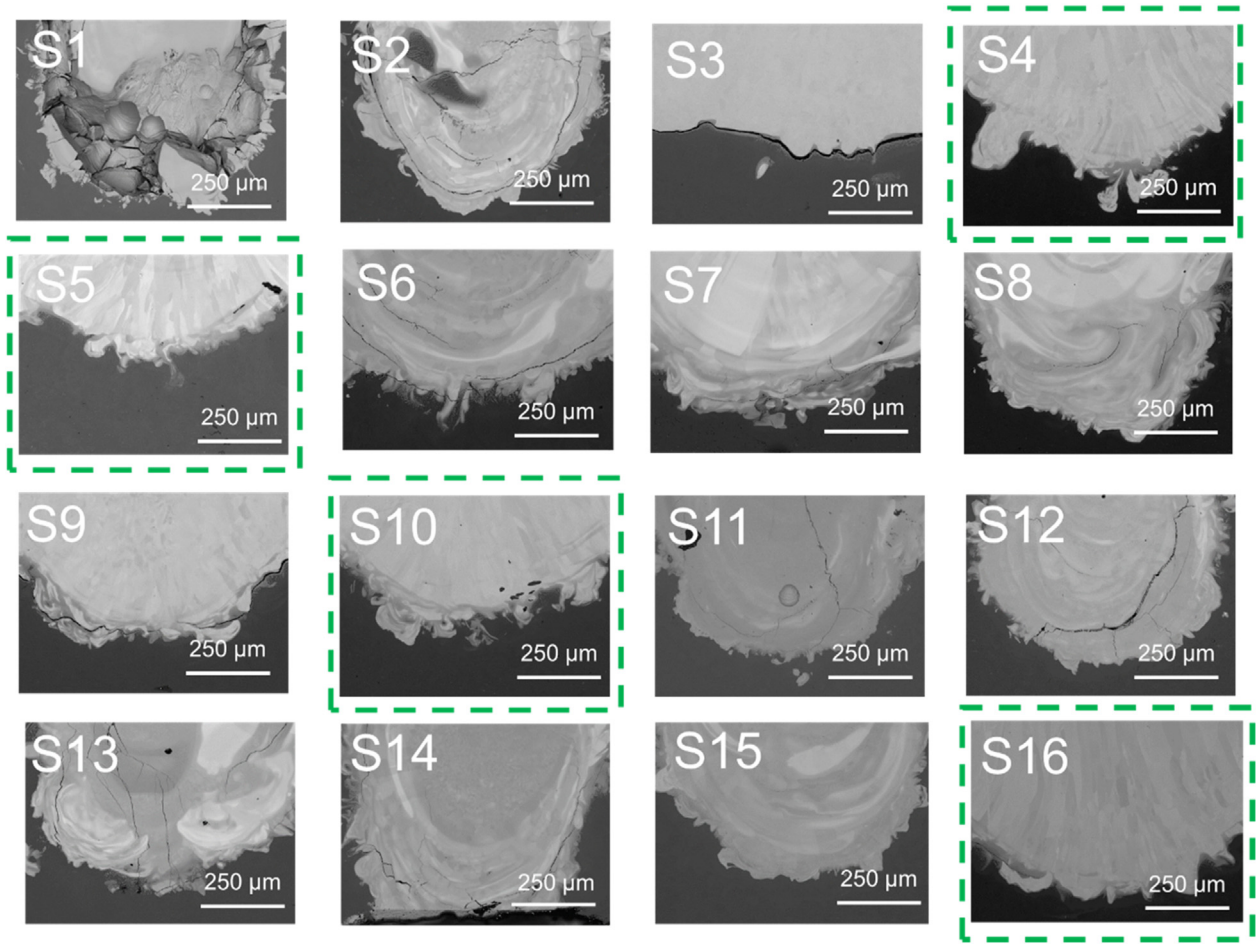

Fig. 5 – High magnification SEM micrographs for the bottom of each samples weld pool. Each image clearly shows any cracks, IMCs and weld pool homogeneity. Samples S4, S5, S10 and S16 highlighted in green show uniform and continuous interfacial IMCs.

using SEM micrographs which assessed the KPIs listed in Section 2.4. The interfacial IMCs and total cracking are two important criteria not only for mechanical properties of joint but also in terms of repeatability of the weld quality and formation of a consistent metallurgical bond between the steel and Al sheets. Figure 4 shows the weld pool cross section shape changes obtained for different welding process parameters. Mainly, two distinct weld pools were observed, one which had large non-uniform interfacial IMCs, excessive cracking at the interface and within the weld pool, and a non-uniform chemical composition within the weld pool which was determined by the intermediate greyscale (compared to the steel and Al) within the weld pool. The other type of weld pool had a much smaller and uniform interfacial IMC layer, with little to no cracking at the interface or in the weld pool. The composition of this type of weld was also uniform. These two distinct shapes of the weld pools observed, depending on the parameters used for welding, which determine the weld penetration and eventually the fusion area chemical composition and its stability.

Upon SEM image analysis of the welded cross sections, six samples (S3, S4, S5, S9, S10, and S16) experienced conduction mode welding (when the total weld width (W_E) is typically larger than the total penetration depth (D), $W_E > D$) and the remaining ten samples experienced keyhole mode welding ($D > W_E$). The results of weld depths are presented in Fig. 6(a) and (b) with respect to the power density (MW/cm^2) for each individual welded sample. The graphs show that there are two distinct classes, conduction (blue) and keyhole (red) mode welded samples. Within the keyhole mode welded samples there are three sub-classes, class 1 and 2 are S (6, 11, 12, 14) and S (7, 8, 12, 14), these two classes are distinguished by their weld depths. The third class are the two outliers S1 and S2, which may be due to their high (est) speeds of all welds (3.3 m/min) or more likely their considerably lower focal offsets, 5 and 10 mm, respectively.

It is reported that a transition from conduction to keyhole mode laser welding occurs at about 1 MW/cm^2 in steel [48]. At power densities at or below 0.1 MW/cm^2 conduction mode is prevalent due to only less than 30% of the laser light being absorbed by the surface (through Fresnel absorption) and the rest being reflected, this in turn results in a shallow weld penetration [48]. In the current study the conduction mode samples were all produced at power densities in the range of

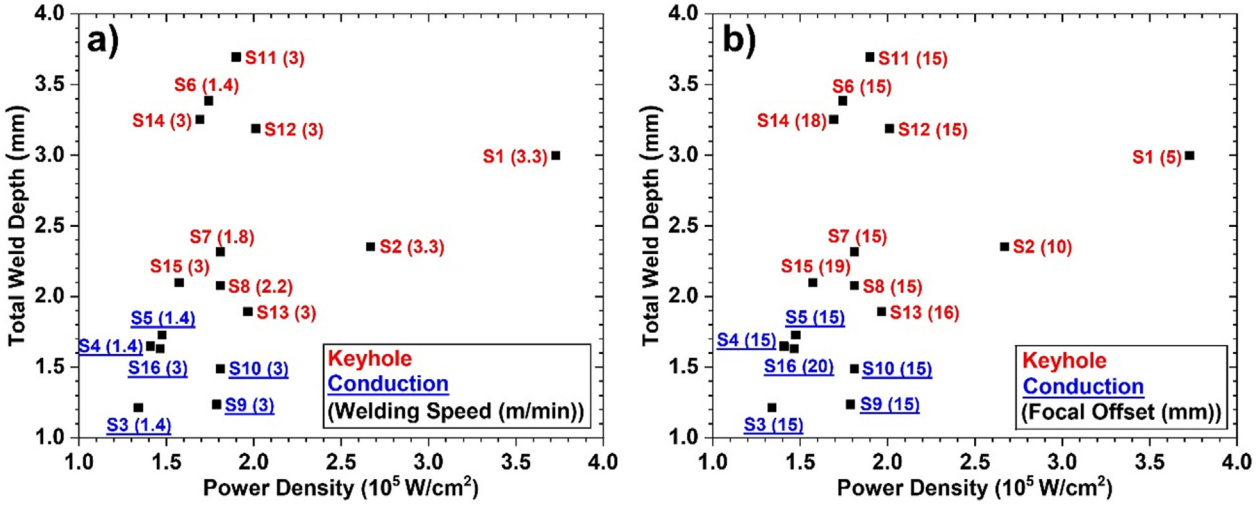

Fig. 6 – A plot of total weld depth vs power density, highlighting the mode of welding for each of the samples (points), as conduction or keyhole. (Welding speed (S_x) annotated in (a) and focal offset (A_z) annotated in (b)).

0.13–0.18 × MW/cm^2, keyhole samples were produced at power densities of 0.17–0.37 × MW/cm^2. A small overlap between energies is shown between the two welding modes, and it should also be noted keyhole sample S15 had a power density of 0.16 × MW/cm^2, but was the only keyhole welded sample (of 10) which had an intensity significantly lower than that of 0.17 × MW/cm^2. The bracket annotations in each of Fig. 6(a) and (b) show the welding speed (S_x) and focal offset (A_z), respectively. It can be seen in both graphs, keyhole samples S1 and S2 (which have the largest power densities) have the highest S_x and lowest A_z and conduction mode samples S3, S4 and S5 have the lowest S_x and intermediate A_z values. Additionally, based on observations, conduction mode welded samples which had depths shallower than 225 μm in the Al side (i.e. samples S3 and S9) are not desirable because they can easily result in continuous cracks at the welding interface which can be seen in the SEM micrographs in Fig. 5. Therefore, the transition from excessively (continuously) cracked welds to crack free welds mainly takes place by reducing the mixing of Fe into Al during the welding and ultimately suppressing the interfacial IMCs with adequate penetration of liquid steel.

Figure 7(a) shows the relationship between the IMC thickness of each of the samples and the weld penetration depth into the Al sheet. A clear difference can be seen between the conduction (blue) and keyhole (red) mode welded samples in the form of two classes. The conduction mode samples had a max Al sheet penetration of ~550 μm and a max IMC thickness of 98 μm (with a standard deviation of 7.9 μm). It should also be noted 9 of the 10 keyhole samples had a fixed amount of

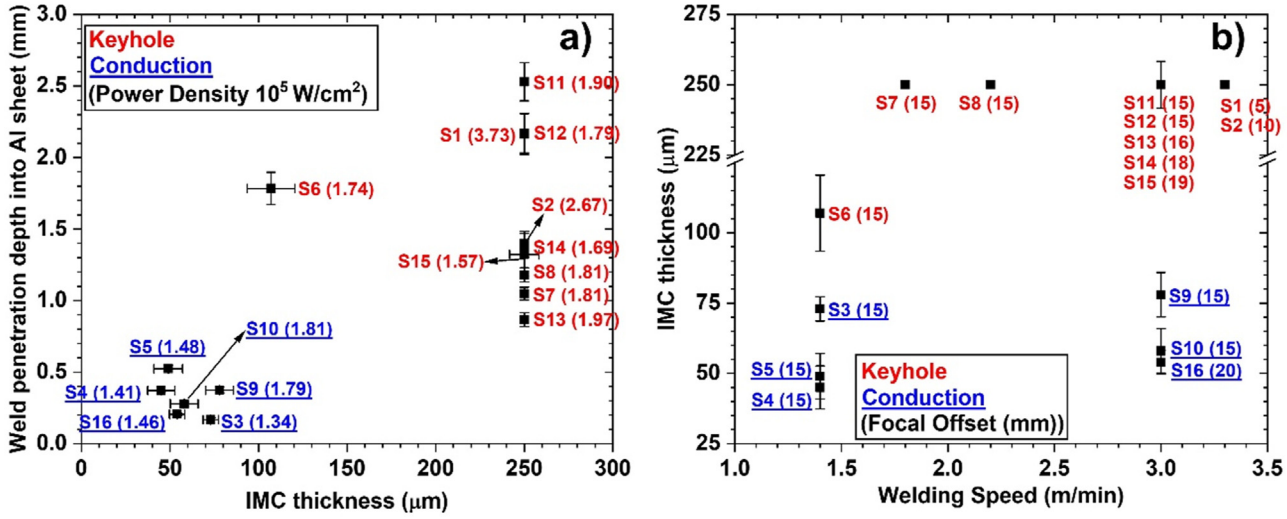

Fig. 7 – Plots of (a) IMC thickness vs weld penetration depth (into Al sheet) with power density annotated and (b) welding speed (S_x) vs IMC thickness with focal offset (A_z) annotated. (Note: 9 of the 10 keyhole samples had a fixed amount of 250 μm for the IMC thickness, this is due to the actual thickness being excessively large to quantify).

250 μm for the IMC thickness, this is due to the actual thickness being excessively large to quantify. Only sample S6 had an IMC thickness of (well) below 250 μm at an amount of 107 μm, it is interesting to note sample S6 also was the only keyhole sample to use a welding speed (S_x) of 1.4 m/min, which matches with the most ideal conduction mode sample S4 (Fig. 7(b)) they also had the same focal offset (A_z) of 15 mm. The clear difference between S4 and S6 being the power density (Fig. 6) which in turn creates the keyhole welded sample rather than the conduction mode as mentioned previously and stated in literature [48]. Furthermore, the number of cracks in S6 was also the least from all keyhole mode samples, this can also be seen in Figs. 4 and 5 and the summary of the microstructural features' quantification Table 4.

The interfacial IMCs thickness and number of cracks within the melt pool for various welding conditions are quantified in Fig. 8. The error bars presented in graphs correspond to the spread (standard deviation) within the weld pool, three cross sections of each weld pool sample were used for analysis in order to improve the representativeness. A comparison of the IMCs thickness and number of cracks (Fig. 8(a)), shows that the thickness of IMCs and number of cracks are less in samples S4 and S5 (sample S3 is disregarded as indicated earlier due to shallow welding depth). In Fig. 8(b), the heat affected zone (HAZ) is larger in the steel side (approximately 400–650 μm in size) in comparison with the Al side (approximately 100–200 μm in size). Due to the one-sided nature of the laser welding technique, the fusion zone has an asymmetric shape such that the volume of the weld metal in the upper sheet side is larger than that of the lower sheet side. Despite the asymmetrical shape of the weld pool, varying laser absorptivity and thermal conductance properties of the two base metals lead to differences in the heat absorption and dissipation which in turn, affected the weld pool and HAZ thickness. A summary of the weld characteristics measured for all the samples is shown in Table 4. Overall, sample S4 shows optimal characteristics. It should also be noted that samples with excessive IMC growths were given a fixed figure of 250 μm, which was the minimum IMC thickness from all the nine samples.

3.2. *Composition and microstructure analysis*

A distinct variation in keyhole and conduction welding mode samples was observed with regards to weld geometry and depth. With regards to the KPIs measured in Table 4 Sample S4 was the optimal within the six conduction mode samples, and sample S6 was the optimal within the nine keyhole mode samples. S1 was a far sub-optimal keyhole mode sample with regards to the KPIs. Each of the three samples showed three levels of IMC thicknesses, and cracking (Table 4). With S4 showing the least IMC thickness and cracking and S1 showing the most IMC thickness and cracking. As mentioned previously this transition from excessively cracked to crack free, is due to the mixing of the Fe and Al during the welding process, therefore, in order to investigate this by using S1, S6 and S4 a series of μ-XRF maps and subsequent line-scans were performed. Fig. 9 shows the μ-XRF derived chemical maps for the Al and Fe elements for samples S1, S6 and S4, respectively, it should be noted the wt.% scale was set to 0–10% in order to

Table 4 – Summary table of the average key performance indicators measured through image analysis of SEM micrographs from three cross-sections (Figs. 4 and 5). (Single standard deviation given in brackets).

	Sample ID														
	S1	S2	S3	S4	S5	S6	S7	S8	S9	S10	S11	S12	S13	S14	S15	S16
Interfacial IMC thickness [μm]	250*	250*	73 (4.3)	45 (7.6)	49 (8.1)	107 (13.5)	250*	250*	98 (7.9)	58 (7.9)	250*	250*	250*	250*	250*	54 (4.3)
Chemical Composition	N	N	U	U	U	U	U	N	U	U	N	N	N	N	N	U
Number of cracks	–	–	4 (2)	3 (1)	2 (1)	9 (2)	–	–	5 (2)	4 (1)	–	–	–	–	2 (2)	1 (1)
Total weld width [μm]	2374 (70)	2491 (34)	1971 (156)	2440 (104)	2946 (122)	3147 (549)	2729 (123)	2191 (158)	2047 (152)	2697 (262)	2340 (156)	3188 (210)	2905 (72)	3044 (289)	2448 (162)	2153 (163)
Total weld depth [μm]	2997 (168)	2353 (136)	1215 (213)	1648 (256)	1727 (143)	3385 (430)	2316 (278)	2078 (253)	1236 (156)	1490 (163)	3695 (231)	3187 (356)	1894 (96)	3254 (289)	2100 (114)	1629 (210)
Aspect ratio and welding mode	0.79 K	1.06 K	1.62 C	1.48 C	1.71 C	0.93 K	1.18 K	1.05 K	1.66 C	1.81 C	0.63 K	1.00 K	1.53 K	0.94 K	1.17 K	1.32 C
HAZ thickness (steel side/ Al side) [μm]	464 (94)/ 123 (23)	475 (32)/ 163 (19)	536 (41)/ 123 (7)	503 (52)/ 123 (22)	589 (23)/ 157 (20)	662 (36)/ 200 (29)	498 (47)/ 130 (23)	467 (39)/ 158 (26)	426 (44)/ 134 (12)	523 (62)/ 107 (12)	456 (53)/ 128 (12)	623 (48)/ 152 (20)	648 (63)/ 147 (24)	549 (52)/ 189 (21)	593 (59)/ 156 (14)	675 (72)/ 137 (13)

Note: U, uniform; N, non-uniform; C, conduction mode; K, keyhole mode.
* An IMC thickness of 250 μm is assumed due to the excessive amount of IMCs.

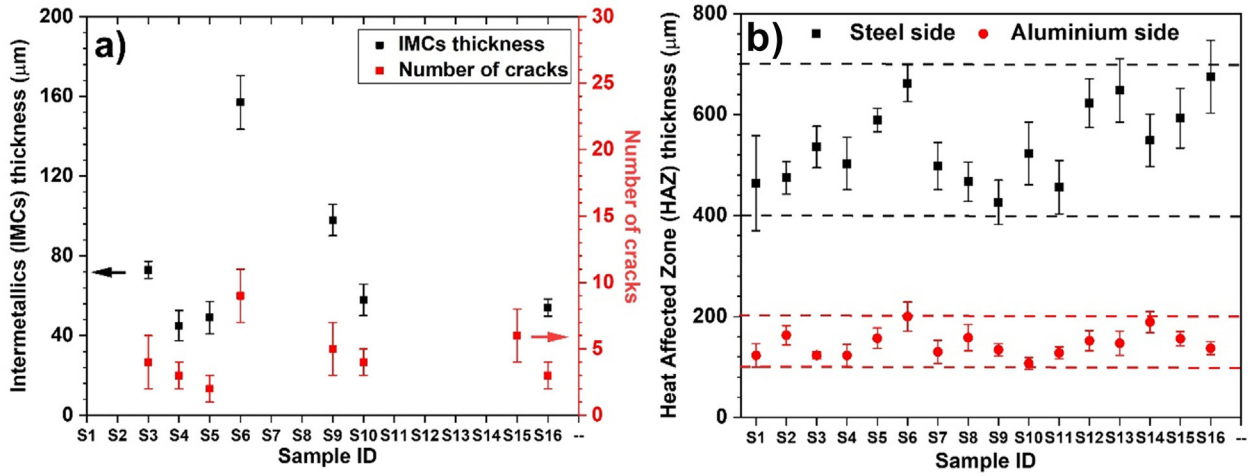

Fig. 8 – Quantitative analysis of each welded sample as listed in Table 3: (a) IMC thickness and number of cracks, and (b) thickness of heat affected zone (HAZ) in the Steel and Al side. Note: In figure (a) data is not presented when the weld pool showed significant number of cracks and IMCs (i.e., S1).

show the mixing of the elements. It is clear for the conduction mode sample S4 (Fig. 9(c) and (f)) that there was little to no mixing of the Fe and Al within weld pool. It is worth mentioning from hereafter no mixing will refer to the mixing of the Fe and Al close to the interface only (> 100 μm, conduction mode, for example S4), and mixing will refer to large amount of Fe and Al mixing within the weld pool (keyhole mode, for example S6). Whereas for the two keyhole mode samples, S1 and S6, there was indeed mixing of the two elements within the weld pool, for which it was more excessive in sample S1 as can be seen in Fig. 9(a) through the darker weld pool verses the slightly lighter weld pool for sample S1 in Fig. 9(b). The μ-XRF derived line-scans were also performed at a thickness of 0.2 μm down the centre of the weld pool, marked by the red arrow in each of the figures. The profiles for Fe and Al are shown in Fig. 10 for each of the samples. Once

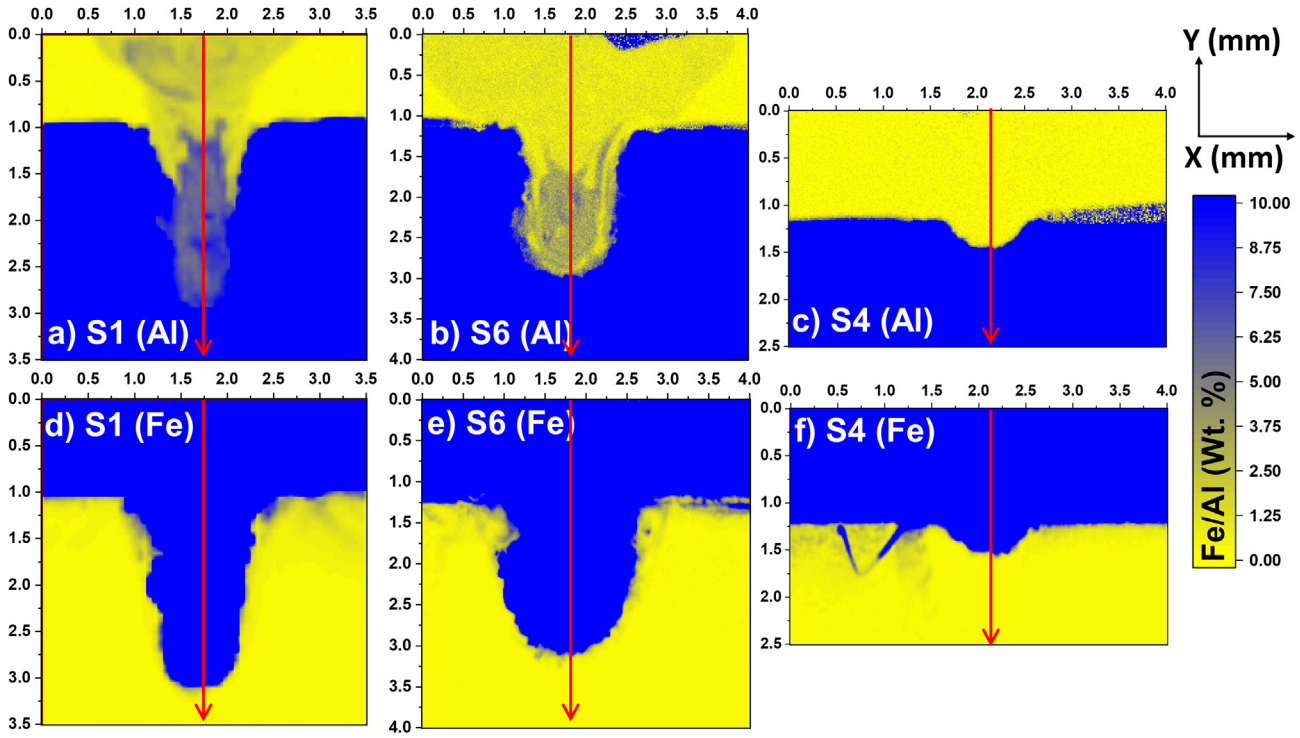

Fig. 9 – μ-XRF derived chemical maps for Al and Fe for samples S1 (a and d), S6 (b and e) and S4 (c and f), red arrows indicate position and direction of line scan, wt.% are limited to 0–10% to show mixing of elements.

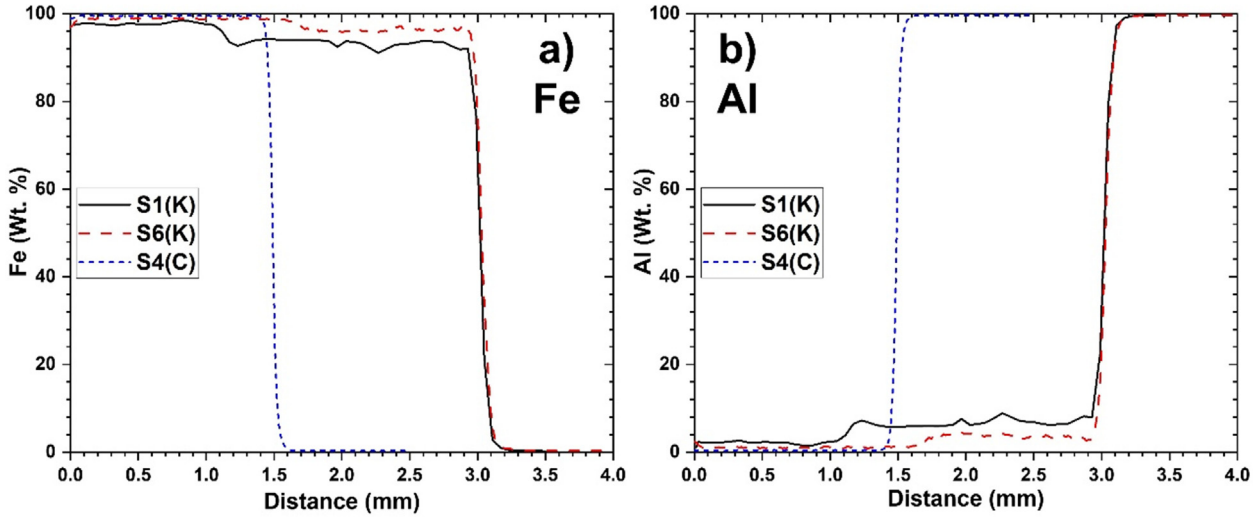

Fig. 10 – μ-XRF derived line-scans for Al and Fe for samples S1, S6 and S4, showing the full range of wt.%.

again, the conduction sample S4 showed mixing only at the interface which can be seen through the 100 to 0 and 0 to 100 transitions in composition. Whereas keyhole sample S6 showed an intermediate amount of mixing and sample S1 showed the greatest amount of mixing with up to 10 wt.% of Al mixing into the weld pool. This explains the excessive amount of IMC growth and as a result excessive cracking in the sample (S1), as compared to sample S4 with little to no cracking. In a study by Huang et al. [49] of Cu and Al mixing, EDS mapping was used to detect and quantify the mixing of Cu and Al based on variable welding parameters for keyhole mode welding. It was found that the high laser power increased the recoil pressure which forced the Cu up into the weld pool, the Marangoni effects also initiated vortices which facilitated further mixing. By simply comparing the power figures used for the three samples in Table 3, the conduction mode sample S4 used the lowest power (3780 W), keyhole mode samples S1 and S6 used powers of 4860 W and 4680 W, respectively, which match conclusions from the study in [49]. When taking into consideration the beam spot sizes (i.e. power density Fig. 6), the same relation is shown.

The conduction mode sample S4 showed the best characteristics with regards to the least IMC thickness, and least cracking (from all the samples in this study). Therefore, in depth microstructural characterisation was focussed on this sample weld cross sections, which were analysed in detail by using high-resolution electron microscopy techniques. It is also worth noting that compared with other dissimilar welding published literature [23,24], the current work has produced little to minimal cracking by RLW, of which conduction sample S4 is a good example.

Fig. 11 compiles representative results obtained from EBSD and EDX measurements for sample S4. It can be seen in the EBSD maps (Fig. 11(a)) that there are multiple grain sizes within the fusion zone from large columnar grains within the top sheet (Steel) towards the finer grain sizes within the last solidified area, i.e., at bottom of the fusion area. Long columnar grains are formed due to directional heat transfer under a severe temperature gradient (arising out of high heating and cooling rates). The EBSD maps reveal that these columnar grains exhibit <001> fibre texture. The last solidified area close to the Al interface showed coarse equiaxed grains approximately around 120 μm in size through visual observations. This columnar-to-equiaxed transition may have been achieved because of the sufficient constitutional supercooling occurring due to the presence of Al solute, which allows heterogeneous nucleation events in constitutional supercooling zones. The role of solute in grain refining explain in Ref. [50,51]. It is also worth noting that compared with conduction mode welding, keyhole mode welding contains larger amounts of Al solute within the weld pool. This can be seen in Figs. 4 and 5 through the darker weld pool in the keyhole mode welds. The increased solute concentration delivers higher constitutional supercooling faster and therefore, the grain size within the fusion zone is smaller but at the same time it also forms a larger volume of IMCs and cracks, as shown in Fig. 4.

The fusion zone on the Al side contains a very uneven IMC region, which can be identified by combining EBSD and EDS to show simultaneously composition and crystallographic variation, an example, as shown in Fig. 11(a). As welding transfers from conduction to keyhole mode, the IMCs thickness increases and can be seen throughout the fusion area (Al side) with non-uniform distribution as shown in Fig. 5. Fig. 11(c) shows that the η-Al_5Fe_2 phase accounts for the majority of the reaction layer with the columnar grain structure. The η phase develops a fibrous structure with the <001> direction preferentially orientated in the direction of columnar growth (i.e., normal to the interface plane), what was also observed in other work [7]. The chemical composition of the reaction layer was measured by EDX along the line indicated by the red colour in Fig. 11(b). EBSD Kikuchi patterns in Fig. 11(c) confirmed the presence of η-Al_5Fe_2 and two other types of IMCs that consisted of discontinuous layers of κ – $AlFe_3$ and θ – $Al_{13}Fe_4$. These two distinct layers were indexed by EBSD. The EDX was used to measure the Fe-to-Al ratios, which were

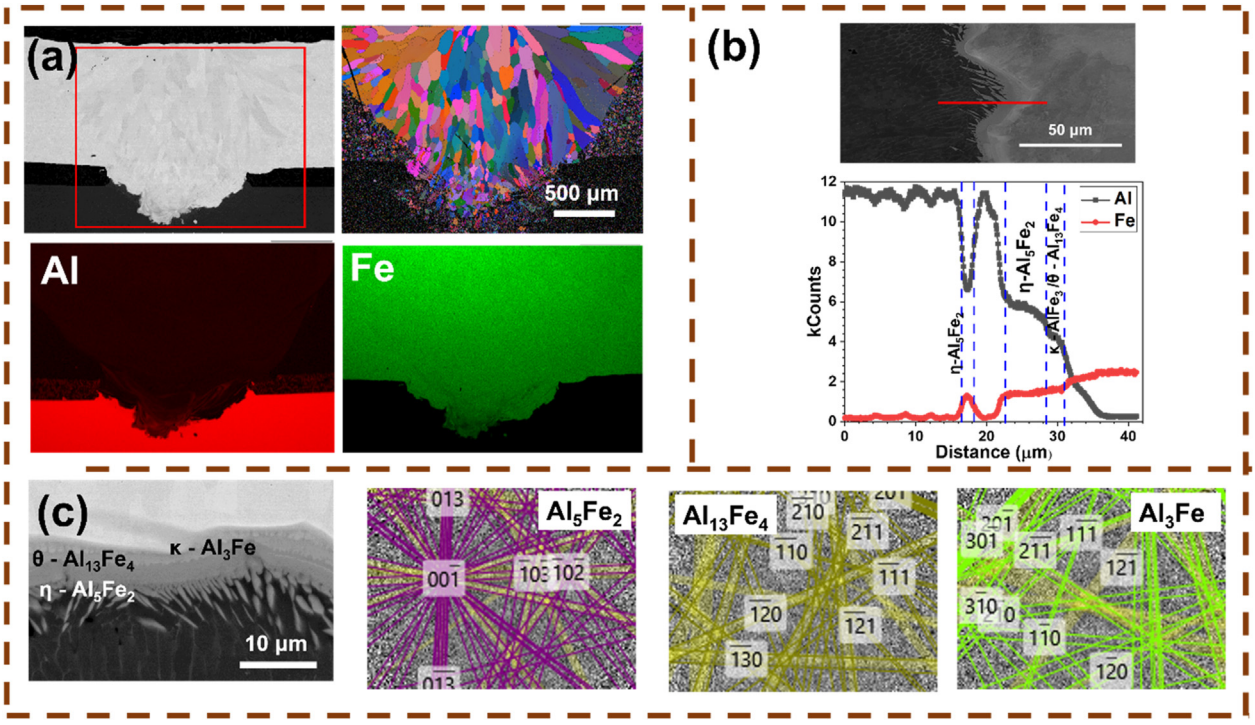

Fig. 11 – SEM analysis of the weld pool of sample S4 (a) EBSD and EDS maps, showing columnar grain growth in the weld pool and IMCs, (b) EDS line scan result obtained along the red line; and (c) EBSD Kikuchi patterns identifying three IMCs phases at the steel-Al interface: η-Al_5Fe_2, θ – $Al_{13}Fe_4$, and κ – $AlFe_3$.

consistent with the compositions of κ – $AlFe_3$ and θ – $Al_{13}Fe_4$. On the Al side, the HAZ area also showed precipitated eutectic phase Al_3Fe, which mainly occurs through diffusion of Fe. Springer et al. [7] noted the presence of Zn on these IMCs, however, in this study no other alloying elements within the IMC reaction layers were detected in any of the welds. It can be concluded that the Zn coating on the steel evaporated during the welding process.

In the keyhole mode welding (i.e., S1), two additional observations were made: (i) excessive cracking and a non-uniform weld pool with rich segregation which can be seen in Figs. 9 and 5; and, (ii) thick IMC layers as shown in Fig. 5. The observed cracks in S1 as shown in Fig. 12 and can be classified as: (i) solidification cracking (which is caused by to hot tearing); and (ii) cold cracking (caused by the stresses generated through welding). Fig. 12(a) which shows solidification

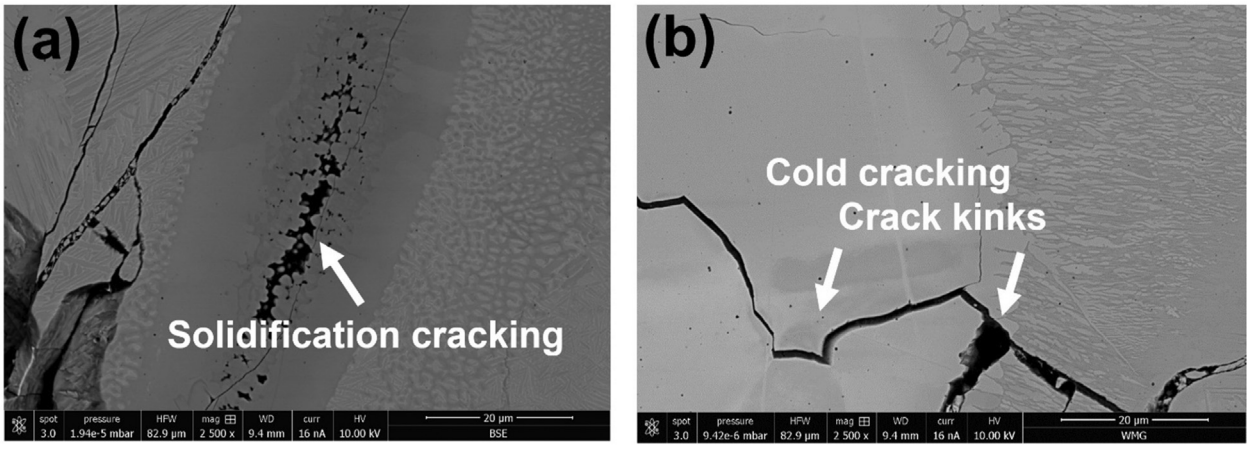

Fig. 12 – The two types of cracks observed in the keyhole melting weld pool (sample S1 used here): (a) solidification cracks, primary dendritic structure evident in micrograph which indicates that crack initiated at last stage of the solidification, (b) the majority of cracks are cold cracks, some of cracks may have initiated through solidification and later propagated at later stages through several grains or IMCs. Crack sizes are observed from a few microns to few mm in length. Note: In the current work, liquation type cracking has not been observed, which is through segregation of elements on grain boundaries.

cracking, displays the almost spherical features of cells and dendrite arms, this confirms separation occurred whilst little remaining liquid was still present. Furthermore, that there was insufficient feeding of the remaining liquid in order to accommodate the solidification shrinkage strain within the region. Moreover, during the solidification process a few microns sized AlFe IMCs had formed. These AlFe IMCs are seen within the intercellular regions and prevent feeding of the remaining liquid to that region. Typical solidification cracking leaves large gaps between the two surfaces of interest, usually with a very irregular morphology and not matching contours as seen in Fig. 12(a). This observation of solidification cracking together with the identification of AlFe IMCs leads to a possibility that the formation of the AlFe IMCs caused the solidification cracking.

Fig. 12(b) shows the cold cracking, unlike solidification cracking, cold crack is easily distinguishable through metallography as it does not possess characteristics such as exposed dendrites. The cracked surfaces typically have matching contours and look like a jigsaw puzzle border line. Additionally, the edges are usually clean without any unevenness and often contain sharp kinks (as sharp as 90°). A typical cold crack length is from a few microns to a few millimetres and are significantly larger than solidification cracks. Although, not all long cracks are generated due to solid state cracking mechanism but could also result from the propagation of cracks that nucleated as hot tears during the solidification process.

3.3. *High speed imaging*

To better understand the metallurgical changes occurring in the conduction and keyhole modes during the welding, high-speed digital imaging was used. Fig. 13 and the video (supplementary movie) shows the dynamics of the laser welding process, for samples S1 (keyhole mode) and S4 (conduction mode). The displayed characteristics of the welding process include the front and rear melt pool walls, keyhole or conduction modes, and mushy zones as shown in Fig. 13, and inlet, spatter, vapour flow and plume as can be seen in the video (supplementary movie). The main differences between the conduction and keyhole welding modes can be seen in the melt pool size, solidification process and splashing of the molten droplets.

Supplementary video related to this article can be found at https://doi.org/10.1016/j.jmrt.2022.05.041

The conduction mode of welding is presented in (Fig. 13(b)). As the laser beam is radiated onto the steel (Fe) surface, the steel is heated to the melting point, the penetration of this molten steel into the weld is determined by the rate of intake of energy from the laser and the out take of energy through the combined thickness of the metals (Fe and Al) via conduction. This energy balance is governed by the power density of the laser beam. As mentioned previously the mode of laser welding (keyhole or conduction) is dependent on the power density which determines the amount of energy which is absorbed or reflected [48]. The evaporation of metal during the welding process allows a deep penetration of laser beam owing to the strong recoil pressure of vaporisation. However, the upward flowing vapour met the downward flowing vapour at the bottom of the keyhole, the whirlpool of vapour was generated which can be seen in Fig. 13(a). It is noticeable from the weld cross section and video snapshot that many weld defects, such as spattering, loss of molten material becomes more severe with the increasing penetration depth. In

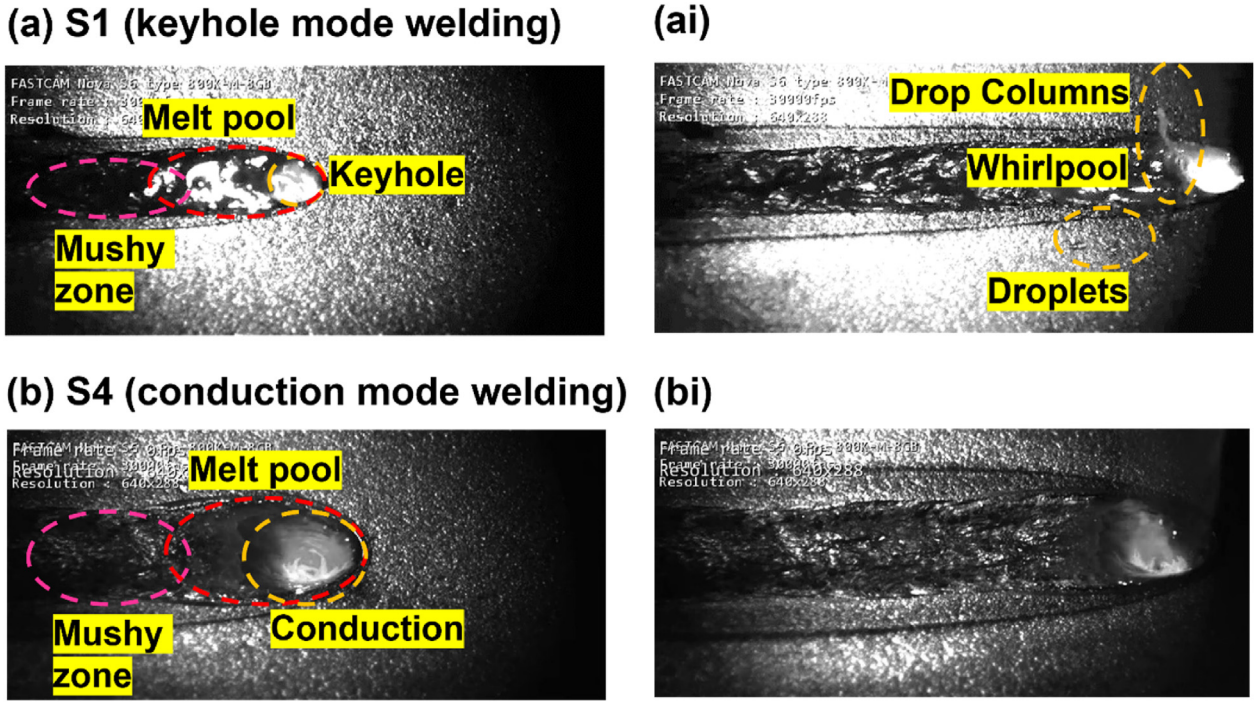

Fig. 13 – Weld pool phenomena observation by using a high-speed imaging camera (a and ai) keyhole mode (sample S1) and (b and bi) conduction mode (sample S4).

addition, a deeper welding depth during keyhole mode results in greater turbulence which leads to an increasing mixing of Fe and Al (Fig. 9), and as a result this facilitates the excessive growth of IMCs and also initiates cracks. Additionally, the recoil pressure and Marangoni effect induce substantial forces on the molten weld pool causing high mobility and vigorous motion of the molten material, this in turn results in unevenness of the IMCs which form.

The keyhole wall temperature and associated recoil pressure increase as the laser power increases. Furthermore, as the welding speed increases, less heating time is available for the laser to heat the liquid to be accelerated (by recoil pressure and increased Marangoni forces).

In conjunction, these two effects, laser power and welding speed determine the velocity of the upward flow, which positively correlates with amount of Al that can migrate to the top region of the molten pool (also seen in Fig. 9 through the μ-XRF maps). It is also clear from the micrographs and video snapshot that under the conduction mode welding the weld pool is less mobile than during keyhole mode welding, with no spattering, this reduces Al mixing with the liquid steel and as a result supresses interfacial IMCs.

3.4. *Mechanical properties*

Lap shear tensile testing was used to measure the weld's failure loads, for a single and double welded joint. With regards to the double welded S4 sample, the second weld was performed outside of the HAZ of the first weld, at a distance of 12 mm. For mechanical tests the sample with the optimum welding conditions was selected (conduction mode sample S4).

Fig. 14(a) shows representative lap shear test results and fracture micrographs. Sample with single weld showed an approximate 4 kN (105.3 N/mm^2) load bearing capacity, compared with 10 kN for 1xxx series Al sheets (without welds). The sample with two welds improved the load bearing capacity by 1.5 times to 6 kN (78.9 N/mm^2), compared with the single welded sample. These results clearly demonstrate that joint strength can be improved by multiple welds if required. However, the strength of the joint did not increase proportionately with the number of weld lines, only the load bearing capacity of the joint increased. Observations made during the tensile lap shear tests revealed that as the sample was pulled it bent outwards, this further induced tensile stress around the weld which encourages pull-out failure mode. It is also observed that significant bending took place in Al sheet in compared with the steel sheet. The sheet with the lower strength tends to bend more than the sheet with the higher strength because during the shear load, the material around the weld ring is more constrained on deformation. In order to understand the failure mechanism, a few lap shear tests were stopped after the load reached to the maximum point (before any failure) and crack initiation was analysed by taking weld cross-sections (Fig. 14(b)). The microstructure micrographs reveal that the crack initiated at the bottom of the weld pool (around the interface between the steel and Al sheets) and propagated through the interfacial IMCs. The microstructure of the double welded samples showed complete failure on the first weld, whereas the second weld was not damaged, this can be seen in Fig. 14(b) where the bottom Al sheet is completely detached in the first weld, but the 2nd weld is completely intact, this improved the overall load bearing capacity. The smaller volume of weld in the bottom sheet (Al) and the higher strength of the upper steel sheet generates a higher strain concentration at the bottom of the weld (which is the weakest point). As loading is continued, strain was localised at the Al plate, initiating cracking at the AlFe rich area and propagating through the interfacial IMC region, which is brittle in nature, in addition to having many inherent micro-cracks. It is also worth noting that in literature, dissimilar metal welding has reported IMCs above a thickness of 10 μm to be considered harmful for hardness and brittleness, therefore affecting the mechanical properties for steel-Al laser welded joints [52], however, the current work has produced an average minimum thickness of IMCs of approximately 50 μm with similar reported strengths of other similar studies [16,17]. Ma et al. used galvanized high-strength dual phase steel (DP590) (0.75 mm thick) welded to Al alloy 6061 (1 mm thick) using a 2-pass laser welding process where the first pass vapourised any Zn and the second pass performed the laser

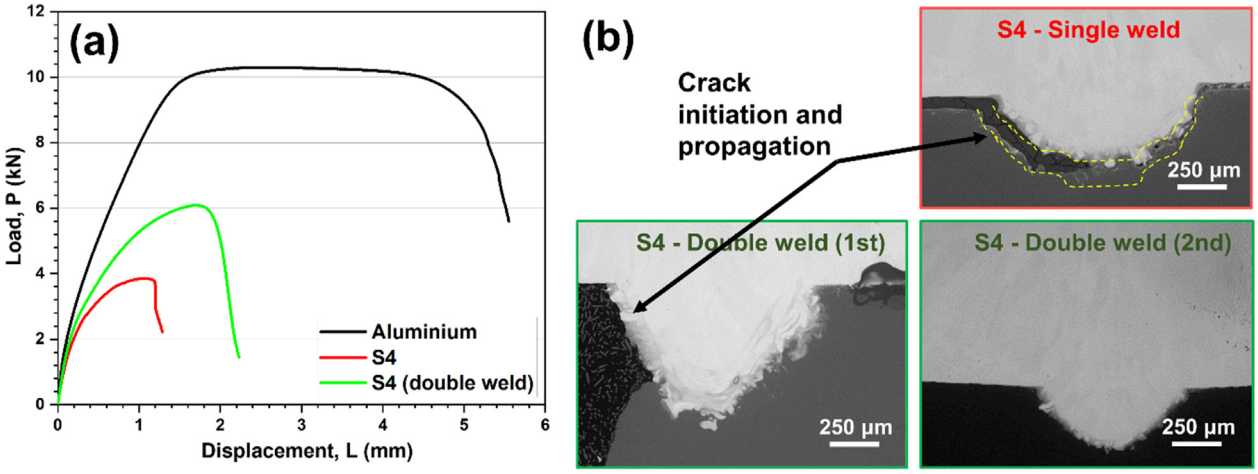

Fig. 14 – Showing (a) Load displacement curves of the optimum condition welded sample, S4 (single and double welds), compared with Al and (b) crack initiation and propagation of cracks through interfacial IMC area. Note: The yellow dashed lines highlights cracked regions in the S4 single weld.

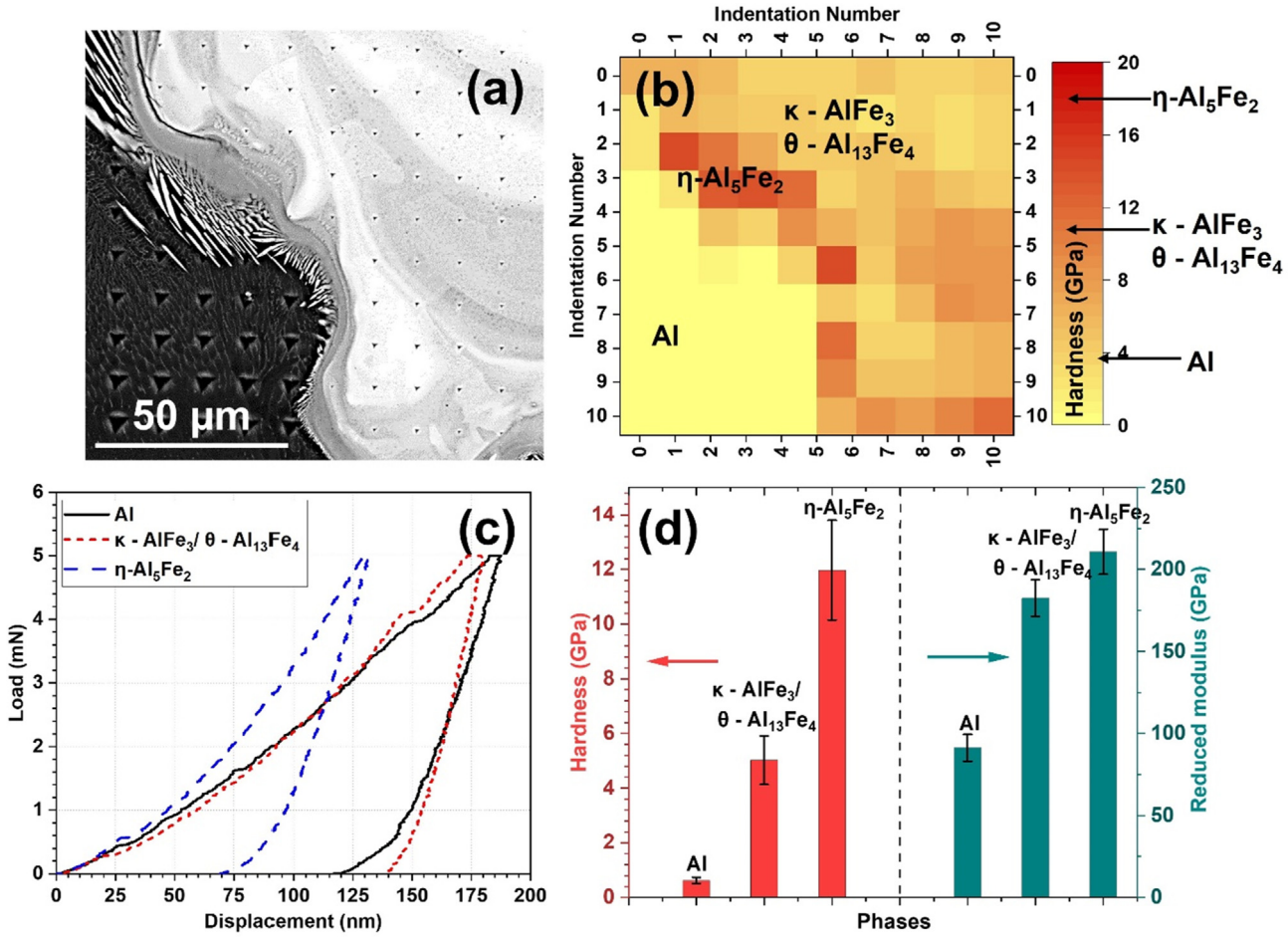

Fig. 15 – Showing results from the nanoindentation test (a) SEM-BSE image of the Al/weld pool interface) where 100 indentations were made, (b) heat map for the acquired hardness, (c) representative load–displacement curves for the different IMC phases, and (d) average hardness and reduced modulus for the different IMC phases.

welding, obtaining a 90.5 N/mm^2 max load amongst all samples tested [23]. Seffer et al. used a range of steels (1.5 mm thick) welded to an Al alloy 6016-T4 (1.15 mm thick) using a lap laser welding process, furthermore, a gap of 0.1 mm was kept for outgassing any vapourised Zn. The maximum tensile shear force achieved in that study was of 42.5 N/mm^2 [24]. In comparison the current work has achieved 105.3 and 78.9 N/mm^2 for single and double seam welded samples.

Nanoindentation measurements were performed to further investigate the interfacial IMCs region between the Al sheet and weld pool. Hardness and elastic modulus values of interfacial IMCs obtained from nanoindentation are presented in Fig. 15. Evidently, from the SEM image (Fig. 15(a)) the lower hardness of the phase showed maximum size and depth of indentation. Individual phase indenter hardness is represented through the heat map (Fig. 15(b)), which further confirms the difference in hardness between the various Al_xFe_x phases, η-Al_5Fe_2, $\kappa - AlFe_3$ and $\theta - Al_{13}Fe_4$ in conduction sample S4. Figure 15(c) shows the load–displacement curves of the individual phases for comparison. The comparison of average hardness and reduced modulus is shown in Fig. 15(d). The η-Al_5Fe_2 IMC shows the highest hardness (11.8 ± 1.8 GPa) and the largest reduction in modulus (210 ± 13 GPa) amongst the three IMCs. The hardness and reduced modulus of the $\theta - Al_{13}Fe_4$ and $\kappa - AlFe_3$ phases are similar and also considerably lower than that of the η-Al_5Fe_2 IMC phase. This results further supports previous results that suppression of the η-Al_5Fe_2 IMC is vital to improve mechanical properties of dissimilar (steel/Al) welding. In a study by Li et al. [35], it was found that the rank of the IMCs hardness was in the following order $Al_3Fe > Al_{15}Fe_2 > Al_{13}Fe_4 > AlFe > Al_2Fe > AlFe_3$, however, with a similar range/variation of the hardness values for each IMC.

4. Summary and conclusions

A systematic approach was adopted for the implementation and optimisation of RLW process in the automotive industry. The relationship between the processing parameters, IMCs, cracks and mechanical behaviour of Zn coated IF steel to 1050 aluminium alloy during the RLW process wasstudied and the results indicate the following:

1. From the experimental approach, the laser beam power (P), welding speed (S_x) and focal offset (A_z) have been varied, which in turn form either keyhole or conduction mode

welds. Between these two modes of welding, there is a significant change in the volume and distribution of AlFe-rich IMCs, number of cracks and weld pool size. Optimum processing conditions were achieved through conduction mode welding at power densities of 0.13–0.18 × MW/cm^2, where the laser energy only melts through the IF steel, and marginally melts the Al sheet, whilst establishing a more uniform and steady fluid-flow in the weld pool - compared to the cases in keyhole mode. This leads to minimisation of excessive mixing of Fe and Al in the weld pool.

2. Detailed characterisation was performed on a specific sample (conduction mode (S4)) which showed optimised processing conditions. In the weld pool, long columnar grains formed due to directional heat transfer under a large temperature gradient and near to the Al interface, coarse equiaxed grains formed in the presence of Al solute. Three main IMCs were identified through SEM-based EDX and EBSD analysis at the interface: η-Al_5Fe_2, $\kappa - AlFe_3$ and $\theta - Al_{13}Fe_4$. The faceted η-Al_5Fe_2 IMCs is the major constituent of the reaction layer, however, these IMCs did not form a continuous layer.
3. Only 1 out of 10 keyhole welded samples did not contain excessive IMC formation (as well as cracking), namely, sample S6. This sample possessed the same speed (1.4 m/min) and focal offset (15 mm) of the ideal conduction mode welded sample S4.. The power density which was of 0.17 × MW/cm^2 vs. the power density of sample S4, 0.14 × MW/cm^2 created the transition from conduction to keyhole. This suggests that the welding speed, S_x of 1.4 m/min and focal offset, A_z of 15 mm is ideal for this steel and Al combination, for the adopted laser system.
4. Based on the μ-XRF mapping, excessive mixing of the Fe and Al, predominantly took place in the keyhole mode samples with very little in the conduction mode samples (i.e., S4). With regards to keyhole mode, the samples with the higher power or power density (i.e., S1) showed the greatest amount of weld penetration depth and therefore, the largest degree of mixing of elements. This led to excessive IMC formation and cracking for those samples. Sample S6 showed intermediate properties with regards to penetration, mixing, IMC thickness and cracking when compared to S1 and S4.
5. The solidification and cold cracks were observed, mainly in keyhole mode welding. Some of the cracks may initiate through solidification cracking and at later stages propagate through several grains or IMCs. In comparison to other recent studies [23,24,41,42,45], this study has produced Steel-Al dissimilar metal welds with very little to minimal cracking with the conduction mode RLW technique.
6. In the optimally processed conduction mode sample (S4) promising lap shear joint strength was shown. The single weld withstood up to a 4 kN (105.3 N/mm^2) load and was further improved by approximately 1.5 times to 6 kN (78.9 N/mm^2) through a double weld. The fracture analyses showed the fracture path was through the weld interface and brittle fracture between the Al and interfacial IMC layer.
7. Among all three IMCs, the η-Al_5Fe_2 IMC showed the highest hardness (11.8 ± 1.8 GPa) and reduced modulus (210 ± 13 GPa), which further confirms that supressing this phase can improve the mechanical performance of the weld.

Declaration of Competing Interest

The authors have no conflicts of interest.

Acknowledgments

This work was partially supported by (1) WMG Centre High Value Manufacturing Catapult, (2) APC15 UK project ALIVE (Aluminium Intensive Vehicle Enclosers) and (3) Innovate UK IDP15 project LIBERATE (Lightweight Innovative Battery Enclosures using Recycled Aluminium Technologies). The authors would like to acknowledge the support provided by the WMG Characterisation Facility partially funded by Higher Education Funding Council for England (HEFCE) and the WMG Centre High Value Manufacturing Catapult. H. R. Kotadia would also like to thank Mr. Tom Moore and Mr. Cameron Bee for helping with the EBSD analysis and nano-indentation testing, respectively.

REFERENCES

[1] Aluminium in cars: unlocking the light-weighting potential. European Aluminium Association; 2020.
[2] Singh M. Application of steel in automotive industry. Int J Emerg Technol Adv Eng 2016;6(7):246–53.
[3] Bhadeshia HKDH, Honeycombe RWK. Steels—microstructure and properties. 4th ed. Butterworth-Heinemann; 2017.
[4] Polmear I, StJohn DH, Nie JF, Qian M. Light alloys. 5th ed. Butterworth-Heinemann; 2017.
[5] Bhadeshia HKDH. Problems in the welding of automotive alloys. Sci Technol Weld Join 2015;20(6):451–3.
[6] Springer H, Szczepaniak A, Raabe D. On the role of zinc on the formation and growth of intermetallic phases during interdiffusion between steel and aluminium alloys. Acta Mater 2015;96:203–11.
[7] Springer H, Kostka A, Payton EJ, Raabe D, Kaysser-Pyzalla A, Eggeler G. On the formation and growth of intermetallic phases during interdiffusion between low-carbon steel and aluminum alloys. Acta Mater 2011;59(4):1586–600.
[8] Li D, Chrysanthou A, Patel I, Williams G. Self-piercing riveting-a review. Int J Adv Manuf Technol 2017;92(5):1777–824.
[9] Papadimitriou I, Efthymiadis P, Kotadia HR, Sohn IR, Sridhar S. Joining TWIP to TWIP and TWIP to aluminium: a comparative study between joining processes, joint properties and mechanical performance. J Manuf Process 2017;30:195–207.
[10] Kotadia HR, Rahnama A, Sohn IR, Kim J, Sridhar S. Performance of dissimilar metal self-piercing riveting (SPR) joint and coating behaviour under corrosive environment. J Manuf Process 2019;39:259–70.
[11] Cavezza F, Boehm M, Terryn H, Hauffman T. A review on adhesively bonded aluminium joints in the automotive industry. Metals 2020;10(6):730.
[12] DebRoy T, Bhadeshia HKDH. Friction stir welding of dissimilar alloys – a perspective. Sci Technol Weld Join 2010;15(4):266–70.
[13] Chen CM, Kovacevic R. Joining of Al 6061 alloy to AISI 1018 steel by combined effects of fusion and solid state welding. Int J Mach Tool Manufact 2004;44(11):1205–14.
[14] Xu L, Wang L, Chen Y-C, Robson JD, Prangnell PB. Effect of interfacial reaction on the mechanical performance of steel to aluminum dissimilar ultrasonic spot welds. Metall Mater Trans 2016;47(1):334–46.

[15] Zhang HT, Feng JC, He P, Hackl H. Interfacial microstructure and mechanical properties of aluminium–zinc-coated steel joints made by a modified metal inert gas welding–brazing process. Mater Char 2007;58(7):588–92.
[16] Zhang W, Sun D, Han L, Gao W, Qiu X. Characterization of intermetallic compounds in dissimilar material resistance spot welded joint of high strength steel and aluminum alloy. ISIJ Int 2011;51(11):1870–7.
[17] Sun Z, Karppi R. The application of electron beam welding for the joining of dissimilar metals: an overview. J Mater Process Technol 1996;59(3):257–67.
[18] Kotadia HR, Franciosa P, Ceglarek D. Challenges and opportunities in remote laser welding of steel to aluminium. In: MATEC web of conferences, vol. 269; 2019. p. 2012.
[19] Wang P, Chen X, Pan Q, Madigan B, Long J. Laser welding dissimilar materials of aluminum to steel: an overview. Int J Adv Manuf Technol 2016;87(9):3081–90.
[20] Kraetzsch M, Standfuss J, Klotzbach A, Kaspar J, Brenner B, Beyer E. Laser beam welding with high-frequency beam oscillation: welding of dissimilar materials with brilliant fiber lasers. Physics Procedia 2011;12(Part A):142–9. https://doi.org/10.1016/j.phpro.2011.03.018.
[21] Lee K-J, Kumai S, Kawamura N, Ishikawa N, Furuya K. Growth manner of intermetallic compounds at the weld interface of steel/aluminum alloy lap joint fabricated by a defocused laser beam. Mater Trans 2007;48(6):1396–405.
[22] Szczepaniak A, Fan J, Kostka A, Raabe D. On the correlation between thermal cycle and formation of intermetallic phases at the interface of laser-welded aluminum-steel overlap joints. Adv Eng Mater 2012;14(7):464–72.
[23] Ma J, Harooni M, Carlson B, Kovacevic R. Dissimilar joining of galvanized high-strength steel to aluminum alloy in a zero-gap lap joint configuration by two-pass laser welding. Mater Des 2014;58:390–401.
[24] Seffer O, Pfeifer R, Springer A, Kaierle S. Investigations on laser beam welding of different dissimilar joints of steel and aluminum alloys for automotive lightweight construction. Phys Procedia 2016;83:383–95.
[25] Chen YC, Gholinia A, Prangnell PB. Interface structure and bonding in abrasion circle friction stir spot welding: a novel approach for rapid welding aluminium alloy to steel automotive sheet. Mater Chem Phys 2012;134(1):459–63.
[26] Wang K-K, Chang L, Gan D, Wang H-P. Heteroepitaxial growth of Fe2Al5 inhibition layer in hot-dip galvanizing of an interstitial-free steel. Thin Solid Films 2010;518(8):1935–42.
[27] Akdeniz MV, Mekhrabov AO, Yilmaz T. The role of Si addition on the interfacial interaction in Fe-Al diffusion layer. Scripta Metall Mater 1994;31(12):1723–8.
[28] Shady MA, El-Sissi AR, Attia AM, El-Mahallawy NA, Taha MA, Reif W. On the technological properties of steel strips aluminized in Al-Si baths. J Mater Sci Lett 1996;15(12):1032–6.
[29] Eggeler G, Auer W, Kaesche H. On the influence of silicon on the growth of the alloy layer during hot dip aluminizing. J Mater Sci 1986;21(9):3348–50.
[30] Denner SG, Jones RD, Thomas RJ. Hot-dip aluminising of steel strip: processing, properties and applications. J Iron Steel Res Int 1975;48(3):241–7.
[31] Nicholls John E. Hot-dipped aluminium coatings. Anti-Corrosion Methods Mater 1964;11(10):16–21.
[32] Kurakin AK. Mechanism of the influence of silicon on the processes of the reaction diffusion of Iron in aluminium. Phys Met Metallogr 1970;30(1):105–10.
[33] Gebhardt E, Obrowski W. Reaktionen von festem Eisen mit Schmelzen aus Aluminium und Aluminiumlegierungen. Z Metallkd 1953;44.
[34] Jia L, Shichun J, Yan S, Cong N, Junke C, Genzhe H. Effects of zinc on the laser welding of an aluminum alloy and galvanized steel. J Mater Process Technol 2015;224:49–59.
[35] Li Y, Liu Y, Yang J. First principle calculations and mechanical properties of the intermetallic compounds in a laser welded steel/aluminum joint. Opt Laser Technol 2020;122:105875.
[36] Wang L, Mohammadpour M, Gao X, Lavoie J-P, Kleine K, Kong F, et al. Adjustable ring mode (ARM) laser welding of stainless steels. Opt Laser Eng 2021;137:106360.
[37] Ceglarek D, Colledani M, Váncza J, Kim D-Y, Marine C, Kogel-Hollacher M, et al. Rapid deployment of remote laser welding processes in automotive assembly systems. CIRP Ann 2015;64(1):389–94.
[38] Franciosa P, Sokolov M, Sinha S, Sun T, Ceglarek D. Deep learning enhanced digital twin for Closed-Loop In-Process quality improvement. CIRP Ann 2020;69(1):369–72.
[39] Chianese G, Franciosa P, Nolte J, Ceglarek D, Patalano S. Characterization of photodiodes for detection of variations in part-to-Part Gap and weld penetration depth during remote laser welding of copper-to-steel battery tab connectors. J Manuf Sci Eng 2021;144(7).
[40] Meco S, Cozzolino L, Ganguly S, Williams S, McPherson N. Laser welding of steel to aluminium: thermal modelling and joint strength analysis. J Mater Process Technol 2017;247:121–33.
[41] Coroado J, Ganguly S, Williams S, Suder W, Meco S, Pardal G. Comparison of continuous and pulsed wave lasers in keyhole welding of stainless-steel to aluminium. Int J Adv Manuf Technol 2021;119:367–87. https://doi.org/10.1007/s00170-021-08226-5.
[42] Shu F, Niu S, Zhu B, Wu L, Xia H, Chen B, et al. Effect of pulse frequency on the nanosecond pulsed laser welded Al/steel lapped joint. Opt Laser Technol 2021;143:107355.
[43] Wang C, Cui L, Mi G, Jiang P, Shao X, Rong Y. The influence of heat input on microstructure and mechanical properties for dissimilar welding of galvanized steel to 6061 aluminum alloy in a zero-gap lap joint configuration. J Alloys Compd 2017;726:556–66.
[44] Cui L, Chen H, Chen B, He D. Welding of dissimilar steel/Al joints using dual-beam lasers with side-by-side configuration. Metals 2018;8(12):1017.
[45] Yang J, Li Y-l, Zhang H. Microstructure and mechanical properties of pulsed laser welded Al/steel dissimilar joint. Trans Nonferrous Metals Soc China 2016;26(4):994–1002.
[46] R.F. Sampaio, J.P. Pragana, I.M. Bragança, C.M. Silva, C.V. Nielsen, P.A. Martins, Electric performance of fastened hybrid busbars: an experimental and numerical study, Proc IME J Mater Des Appl 14644207211043009.
[47] EN ISO 12273. Specimen dimensions and procedure for shear testing resistance spot, seam and embossed projection welds. 2001.
[48] Svenungsson J, Choquet I, Kaplan AFH. Laser welding process – a review of keyhole welding modelling. Phys Procedia 2015;78:182–91.
[49] Huang W, Wang H, Rinker T, Tan W. Investigation of metal mixing in laser keyhole welding of dissimilar metals. Mater Des 2020;195:109056.
[50] Lee YC, Dahle AK, StJohn DH. The role of solute in grain refinement of magnesium. Metall Mater Trans 2000;31(11):2895–906.
[51] Easton M, St John D. Grain refinement of aluminum alloys: Part I. the nucleant and solute paradigms—a review of the literature. Metall Mater Trans 1999;30(6):1613–23.
[52] Schubert E, Zerner I, Sepold G. Laser beam joining of material combinations for automotive applications. SPIE; 1997.